Superior Electron Transport and Photocatalytic Abilities of Metal–Nanoparticle-Loaded TiO2 Superstructures

5 AUTHORS, INCLUDING:

Zhenfeng Bian
Shanghai Normal University
29 PUBLICATIONS   **1,849** CITATIONS

SEE PROFILE

Wonyong Choi
Pohang University of Science and Technology
255 PUBLICATIONS   **23,130** CITATIONS

SEE PROFILE

# Superior Electron Transport and Photocatalytic Abilities of Metal-Nanoparticle-Loaded TiO$_2$ Superstructures

Zhenfeng Bian,[†] Takashi Tachikawa,*[,†] Wooyul Kim,[‡] Wonyong Choi,[‡] and Tetsuro Majima*[,†]

[†]The Institute of Scientific and Industrial Research (SANKEN), Osaka University, Mihogaoka 8-1, Ibaraki, Osaka 567-0047, Japan
[‡]School of Environmental Science and Engineering, Pohang University of Science and Technology (POSTECH), Pohang 790-784, Korea

ⓢ *Supporting Information*

ABSTRACT: Metal–semiconductor nanocomposites have been widely employed for designing efficient optoelectronic devices and catalysts. The performance of such nanocomposites is significantly influenced by both the method of preparation and the electronic and morphological structures of metals and semiconductors. Here, we have synthesized novel nanocomposites containing plate-like anatase TiO$_2$ mesocrystal superstructures and noble metal (Au, Pt) nanoparticles. These metal nanoparticles were preferentially photodeposited on the edge of TiO$_2$ mesocrystals. The electron transport and photocatalytic properties of the novel nanocomposites were subsequently studied. Single-molecule fluorescence spectroscopy measurements on a single particle directly revealed that most of the photogenerated electrons could migrate from the dominant surface to the edge of the TiO$_2$ mesocrystal with the reduction reactions mainly occurring at its lateral surfaces containing {101} facets. The loading of metal nanoparticles on the superstructure of TiO$_2$ was found to greatly improve the photogenerated charge separation efficiency allowing significant (more than 1 order of magnitude) enhancement of the photocatalytic reaction rate in organic degradation reactions. These outstanding features allowed significantly reduced consumption (ca. 10% of that of typical TiO$_2$ nanocrystal samples) of the Au or Pt loading on the TiO$_2$ mesocrystal while maintaining the same photocatalytic activity.
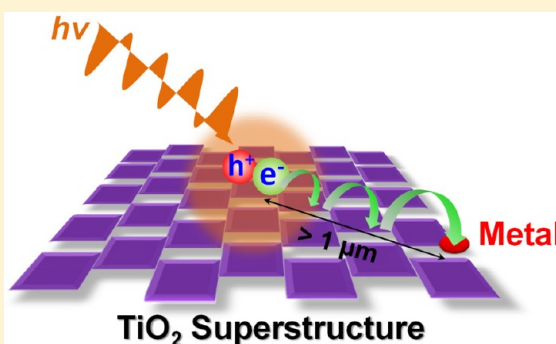
INTRODUCTION

Metal–semiconductor nanocomposites have attracted a great interest since they are widely applied as efficient catalysts in the promotion of a variety of heterogeneous catalytic processes.[1,2] The properties and catalytic performances of such nanocomposites have been known to be strongly influenced by both the method of preparation and the electronic and morphological structures of metals and semiconductors.[3–7] Therefore, the understanding of the composition, size, shape, and location of metal nanoparticles grown on the semiconductor materials would allow optimization of these metal–semiconductor systems leading to improved catalytic performances.

TiO$_2$, owing to its stability, low cost, and nontoxicity properties, is one of the most important semiconductors being commonly used in heterogeneous photocatalysis.[8,9] However, TiO$_2$ presents inherent limitations as a photocatalyst, namely, the rapid recombination of photogenerated electrons (e$^-$) and holes (h$^+$) in both the bulk and on the surface.[10–12] Many attempts have been made to inhibit these charge recombination processes.[13–16] In this regard, an effective way to facilitate charge separation involves the deposition of noble metal (e.g., Au, Ag, Pt) nanoparticles on the TiO$_2$ materials.[17–20] As shown in Figure 1a, the Fermi level and electron accepting states of noble metals locate at an energy level just below the conduction band (CB) of TiO$_2$.[21] Therefore, upon UV light irradiation, the

e$^-$ in the TiO$_2$ CB can be effectively transferred to the metal nanoparticles deposited on the surface, while the h$^+$ remains in the valence band (VB) of TiO$_2$ eventually forming surface reactive radicals and thus avoiding recombination. It was also found that electrons or energies from photoexcited metal nanoparticles are transferred to TiO$_2$ under visible light irradiation.[22–28]

Metal nanoparticles have been most often incorporated onto nanometer-sized TiO$_2$ crystals. The high surface area of TiO$_2$ nanoparticles is expected to provide abundant reaction sites for photocatalytic reactions. However, TiO$_2$ nanoparticles and their aggregates typically present numerous interfacial defects that are undesirable for efficient charge separation since they could act as charge recombination centers.[29] Furthermore, the random aggregation of TiO$_2$ nanoparticles provides poor performances for interparticle charge transfer processes.[30–33] Transient photocurrent measurements and random walk numerical simulations have shown that the ordering of a nanocrystalline structure considerably influences charge transport and recombination phenomena, which are directly related to the performance of photovoltaic cells and photocatalysts
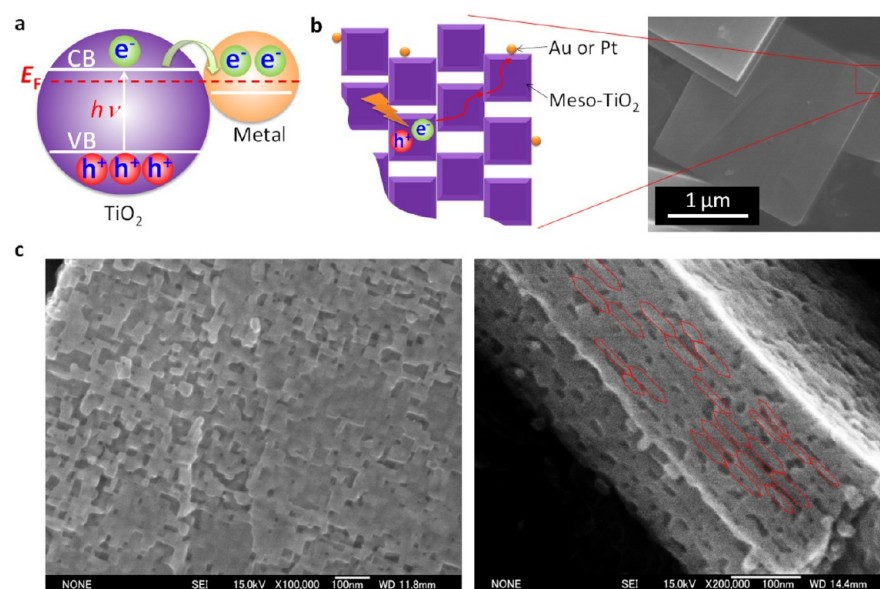
Figure 1. Schematic illustration of (a) electron transfer from TiO_2 to noble metal (Au, Pt) nanoparticles upon irradiation of UV light. (b) Electron transfer on $Au/Meso\text{-}TiO_2$ or $Pt/Meso\text{-}TiO_2$. SEM image in panel b shows the plate-like structure of $Meso\text{-}TiO_2$ composed of an ordered alignment of anatase TiO_2 nanocrystals. The typical size and thickness of $Meso\text{-}TiO_2$ are 2−5 μm and 50−300 nm, respectively.[37] (c) SEM images of basal (left) and lateral (right) surfaces of $Meso\text{-}TiO_2$.

such as those used in water splitting and pollutant degradation.[34,35] Therefore, the design of well-ordered superstructures of TiO_2 combined with noble metal nanoparticles is a promising way to achieve superior photocatalytic activities.

Recently, TiO_2 mesocrystals (i.e., high-surface area, highly ordered superstructures composed of TiO_2 nanocrystal building blocks) have emerged as a new class of porous TiO_2 materials.[36] We have recently demonstrated that anatase TiO_2 mesocrystal ($Meso\text{-}TiO_2$) superstructures largely enhance charge separation upon UV light irradiation showing remarkably long-lived charges and thereby exhibiting greatly increased photoconductivity and photocatalytic activities.[37] As shown in Figure 1b, it might be possible to further facilitate the charge separation in $Meso\text{-}TiO_2$ by incorporating noble metal nanoparticles; although, to the best of our knowledge, there are no comprehensive studies dealing with the preparation and photocatalytic performances of such composites. The plate-like structure of $Meso\text{-}TiO_2$ is composed of an ordered alignment of anatase TiO_2 nanocrystals with dominant {001} facets exposed (Figure 1c). From the side view of $Meso\text{-}TiO_2$ (Figure 1c, right panel), it is clearly seen that small TiO_2 nanocrystals connect with each other to form coherent interfaces.[38,39] Such a superstructure is beneficial in that it allows the migration of the photogenerated e^- between adjacent TiO_2 nanocrystals under UV light irradiation.[37] Furthermore, owing to the efficient interparticle charge transfer of these materials, the amount of noble metal nanoparticles required for effective photocatalysis is expected to be greatly reduced. For example, the ratio of noble metal nanoparticles to TiO_2 nanoparticles in $Meso\text{-}TiO_2$ could be lower than 1 (Figure 1b), whereas higher ratios are typically required for isolated TiO_2 nanoparticles. Because of the high price of noble metals, it is necessary to decrease the cost of noble metal−semiconductor composites for practical applications.

Herein, we used a simple photodeposition method to synthesize Au or Pt nanoparticle-loaded $Meso\text{-}TiO_2$ and subsequently investigated the transport and reaction dynamics

of the photogenerated charge carriers in individual composite materials. The charge mobility in semiconductor materials has already been studied using transient photocurrent measurements or terahertz spectroscopy.[40−42] However, it is difficult to explore the charge transfer processes only by ensemble-averaged measurements because of the inhomogeneous local structures and environments on the nanoparticle surface. In this study, single-molecule (single-particle) microspectroscopy techniques were utilized to determine the location of reactive sites on the different surfaces of $Meso\text{-}TiO_2$. In-site single-molecule reaction analysis on a single particle, owing to its high sensitivity and selectivity and high spatial and temporal resolution, is a very powerful approach for exploring the essential structural and kinetic features hidden in bulk catalysis.[43−45] Surprisingly, it was found that the photo-generated e^- in $Meso\text{-}TiO_2$ could reach the loaded metal nanoparticles over a micrometer distance. Moreover, the metal-nanoparticle-loaded $Meso\text{-}TiO_2$ composites exhibited up to 10 times increased photocatalytic activities as compared to bare $Meso\text{-}TiO_2$ while keeping the Au or Pt content significantly reduced, which is vital for practical applications.

■ RESULTS AND DISCUSSION

As shown in Figure 2, the transmission electron microscopy (TEM) analysis revealed that the Au and Pt ions are reduced and deposited on the surface of $Meso\text{-}TiO_2$. The structural features of $Meso\text{-}TiO_2$ containing 0.04 wt % Au and 1.0 wt % Pt are highlighted in Figure 2a,b, respectively. Selected-area electron diffraction (SAED, insets in the upper left of Figure 2a,b) showed a pattern corresponding to single-crystal anatase along the [001] zone axis. Interestingly, most of the noble metal nanoparticles are deposited on the edge of $Meso\text{-}TiO_2$. The basal surfaces of $Meso\text{-}TiO_2$ are mainly assigned to anatase {001} facets, while the lateral surfaces correspond to {101} facets.[37] Former studies suggested that these {101} facets present higher photocatalytic reduction activities than the {001} facets.[46−49] Photodeposition of Au nanoparticles on the

25445

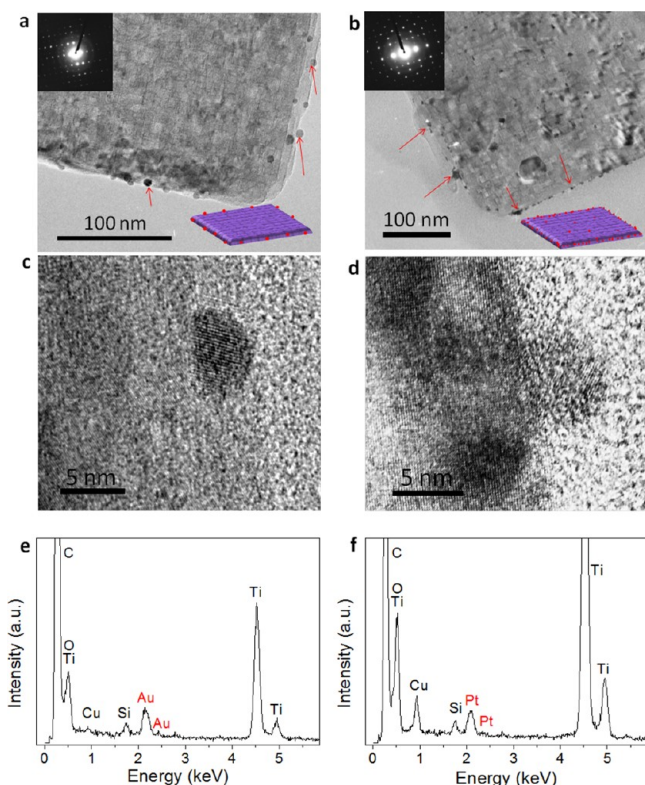dx.doi.org/10.1021/jp309683f | J. Phys. Chem. C 2012, 116, 25444−25453

Figure 2. Transmission electron microscopy (TEM) images of a representative crystal of (a) 0.04 wt % Au/Meso-TiO$_2$ and (b) 1.0 wt % Pt/Meso-TiO$_2$. The selected area electron diffraction (SAED) patterns (inset in the upper left) show the single-crystal diffraction along the anatase [001] zone axis, while the sketches (inset in the lower right) represent noble metal nanoparticles (red dots) loaded on Meso-TiO$_2$ (purple plate). HRTEM images on the edge of (c) 0.04 wt % Au/Meso-TiO$_2$ and (d) 1.0 wt % Pt/Meso-TiO$_2$. EDX spectra of (e) 0.04 wt % Au/Meso-TiO$_2$ and (f) 1.0 wt % Pt/Meso-TiO$_2$ of the selected parts.

micrometer- and nanometer-sized anatase TiO$_2$ single crystals was found not to be size dependent (Supplementary Figure S1). Unlike the thermal treatment that led to an almost homogeneous deposition of metal nanoparticles on all the surfaces of Meso-TiO$_2$ (Supplementary Figure S2), noble metal ions were preferentially photoreduced on the edges of Meso-TiO$_2$ (lower right insets in Figure 2a,b). Therefore, the observed selectivity is presumably dependent on the number of defect sites on the center and edge of the plate as well as the anisotropic electron migration in TiO$_2$.[41] The size distributions of deposited Au and Pt nanoparticles were centered around 3.8 and 3.5 nm, respectively (Supplementary Figure S3). High-resolution TEM (HRTEM) images taken from the edge of Meso-TiO$_2$ revealed the anatase single crystal structure and the Au and Pt nanoparticles (Figure 2c,d, respectively). The single-crystal lattices exhibited atomic (200) or (020) anatase crystal faces with a spacing of around 0.189 nm.[37] The fringes with a lattice spacing of 0.25 and 0.224 nm can be indexed as the (111) planes of Au and Pt, respectively.[20,50] Energy-dispersive spectroscopy (EDS) analysis, simultaneously performed during the HRTEM observations, further confirmed the presence of Au and Pt species on the TiO$_2$ support (Figure 2e,f).

The X-ray diffraction (XRD) patterns of Meso-TiO$_2$, Au nanoparticle-loaded Meso-TiO$_2$ (Au/Meso-TiO$_2$), and Pt nanoparticle-loaded Meso-TiO$_2$ (Pt/Meso-TiO$_2$) powders

revealed a pure anatase structure for all the samples (Supplementary Figure S4a). No diffraction peaks characteristic of Au or Pt were observed because of their small particle size and low loading amounts.[20] The UV–visible diffuse reflectance spectra of Au/Meso-TiO$_2$ and Pt/Meso-TiO$_2$ revealed well-defined absorption bands in the visible region as a result of the plasmon resonance effect (Supplementary Figure S4b).[50,51] The Au/Meso-TiO$_2$ sample exhibited a spectral response in the 450–650 nm wavelength range, while Pt/Meso-TiO$_2$ displayed a broader absorbance covering the whole visible range.

We performed single-particle confocal fluorescence spectroscopy measurements to investigate the recombination of the photogenerated e$^-$ and h$^+$ in TiO$_2$ involved in the photoluminescence (PL) characteristics. Figure 3a shows typical
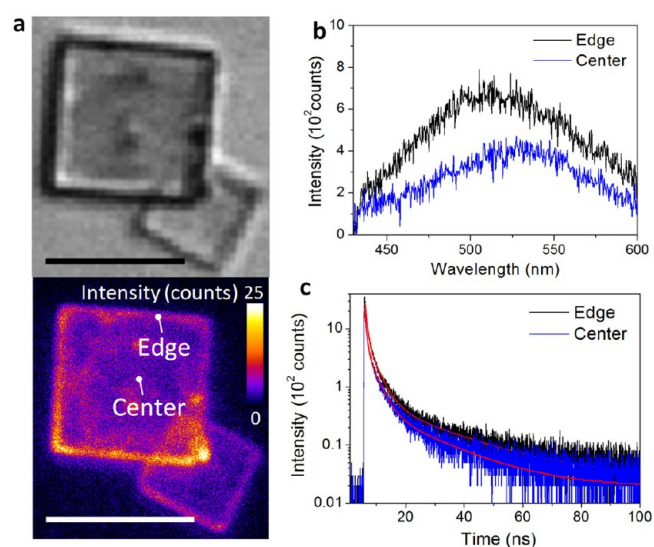

Figure 3. (a) Optical transmission (upper) and emission (lower) images of Meso-TiO$_2$ immobilized on a quartz glass (excitation wavelength, 380 nm; scale bars, 5 μm). (b) Emission spectra and (c) emission decay profiles observed at the center and edge positions on Meso-TiO$_2$. The red curves indicate multiexponential curves fitted to the kinetic trace.

optical transmission and emission images acquired for Meso-TiO$_2$ on a quartz glass upon 380 nm photoexcitation light in ambient air. Emission intensities and lifetimes of Meso-TiO$_2$ at the center and edge positions were significantly different, as shown in Figure 3b,c, respectively. According to the literature,[48,52–55] a broad emission band at around 450–600 nm originates from charges trapped at surface defects of TiO$_2$. The intensity-weighted average lifetime ($\langle\tau_{PL}\rangle$) obtained at the center of Meso-TiO$_2$ was 5.5 ns, which is slightly shorter than that measured at the edge (6.9 ns) (Figure 3c and Table 2). A more significant difference was observed for Meso-TiO$_2$-700 (i.e., Meso-TiO$_2$ annealed under oxygen atmosphere at 700 °C),[37] which showed lifetimes of 6.6 and 15.2 ns at the center and edge regions, respectively (Supplementary Figure S5 and Table 2). The significant difference between emission lifetimes of Meso-TiO$_2$ might be partially produced by the different environments at these particle locations. The refractive index at the center is contributed by one-half from glass and the other half from TiO$_2$, while, at the edge, half of the contribution comes from glass, one-quarter from TiO$_2$, and the other quarter from air. The refractive indexes of glass (n_g), TiO$_2$ (n_T), and air (n_a) are 1.5, 2.5, and 1.0, respectively. According to the

Table 1. Structural Parameters of Photocatalysts

sample	crystalline phase	TiO_2 particle size (nm)	surface area $(m^2/g)^b$	Au loading (wt %)^c	Au particle size (nm)	Pt loading (wt %)^c	Pt particle size (nm)	$N_{Au}{}^e$	$N_{Pt}{}^e$
Meso-TiO$_2$	anatase^a	39^a	63^a	0.04	3.8	0.2	3.5	0.01	0.08
Nano-TiO$_2$	anatase^a	25^a	41^a	0.4 (32%)^d	3.6	4.0	2.8	0.05	0.9
ST-01	anatase^b	7^b	300^b	0.5 (37%)^d	4.0	2.0	4.1	0.005	0.02
ST-21	anatase^b	20^b	50^b	0.4 (43%)^d	5.6	1.6	4.8	0.04	0.2

^{a}From our previous work.[30] ^{b}From manufacturer's specifications. ^{c}Metal loading leading to 50% photoactivity for 4-CP degradation. ^{d}Maximum photoactivities for 4-CP degradation. ^{e}Calculated number of Au or Pt nanoparticles on one TiO_2 particle. $N_{Au/Pt} = V_{total\ Au/Pt} \times V_{one\ TiO2\ nanoparticle}/V_{one\ Au/Pt\ nanoparticle} \times V_{total\ TiO2}$.

Table 2. Kinetic Parameters of the Emission Decay of Meso-TiO$_2$, 0.04 wt % Au/Meso-TiO$_2$, 1.0 wt % Pt/Meso-TiO$_2$, and Nano-TiO$_2$

sample	position	τ_1	τ_2	τ_3	$\langle \tau_{PL} \rangle^a$
Meso-TiO$_2$	center	0.4 ns (65%)	2.2 ns (32%)	14.0 ns (3%)	5.5 ns
	edge	0.5 ns (71%)	2.5 ns (27%)	19.6 ns (2%)	6.9 ns
Meso-TiO$_2$-700 °C	center	0.4 ns (76%)	2.2 ns (22%)	17.4 ns (2%)	6.6 ns
	edge	0.5 ns (75%)	2.4 ns (23%)	33.2 ns (2%)	15.2 ns
Au/Meso-TiO$_2$	center	0.5 ns (79%)	2.4 ns (20%)	12.5 ns (1%)	3.2 ns
	edge	0.5 ns (77%)	2.6 ns (21%)	14.0 ns (2%)	4.3 ns
Pt/Meso-TiO$_2$	center	0.5 ns (73%)	2.3 ns (25%)	10.4 ns (2%)	3.2 ns
	edge	0.4 ns (78%)	2.1 ns (21%)	13.3 ns (1%)	3.3 ns
Nano-TiO$_2$	center^b	0.4 ns (75%)	1.6 ns (21%)	5.7 ns (4%)	2.1 ns

^{a}The multiexponential decay curves were fitted using a nonlinear least-squares method with a multicomponent decay law given by $I(t) = a_1 \cdot \exp(-t/\tau_1) + a_2 \cdot \exp(-t/\tau_2) + \cdots + a_n \cdot \exp(-t/\tau_n)$. The average lifetime $\langle \tau_{PL} \rangle$ was then determined using the equation

$$\langle \tau_{PL} \rangle = \sum_{i=1}^{i=n} a_i \tau_i^2 / \sum_{i=1}^{i=n} a_i \tau_i$$

^{b}The emission lifetime obtained from the center position of an isolated aggregate of Nano-TiO$_2$ (~1 μm size).

equation $\Gamma_{av} = 1/2[n_a/n_T\tau + n_g/n_T\tau]$,[56] the emission lifetime at the edge is expected to be about 1.25 times longer than that at the center. In this equation, τ is the bulk Meso-TiO$_2$ emission lifetime. Another possible explanation for the location-dependent nature of the PL is that charges trapped near the edge are subjected to a different recombination probability as compared to those trapped at the center. Therefore, we deduce that the emission lifetimes and intensities measured near the center are representative of the PL lifetime and intensities of the Meso-TiO$_2$. One typical reference sample (Nano-TiO$_2$) containing a nanometer-sized single crystal with a truncated bipyramid morphology and similar surface area with Meso-TiO$_2$ (Table 1) was chosen for the sake of comparison.[37] Even though PL intensity from a single nanoparticle was too weak to be detected, the emission lifetimes obtained from aggregates of Nano-TiO$_2$ with different sizes were very similar, i.e., 2.1 ± 0.2 ns (Supplementary Figure S6). Shorter (longer) PL lifetimes of the samples indicate a relatively faster (slower) charge recombination process.[52] Thus, since the lifetimes of PL were

greatly extended in the Meso-TiO$_2$ samples, it can be concluded that the mesocrystal superstructure significantly enhances charge separation in TiO$_2$.

Optical transmission and emission images acquired for Au/Meso-TiO$_2$ and Pt/Meso-TiO$_2$ are shown in Figure 4a,b, respectively. A higher PL intensity usually represents a higher recombination rate of photogenerated e^- and h^+ in semiconductors. Au/Meso-TiO$_2$ and Pt/Meso-TiO$_2$ exhibited very weak PL intensities compared to pure Meso-TiO$_2$ under the same experimental conditions (Figure 4c). Therefore, Au and Pt deposition substantially suppressed the radiative charge recombination in Meso-TiO$_2$. Such PL quenching phenomenon has been attributed to the effective trapping of photogenerated e^- by metal nanoparticles.[57] Note that the PL around the center of the Au/Meso-TiO$_2$ and Pt/Meso-TiO$_2$ materials, where the metal nanoparticles are rarely deposited, was also significantly quenched. The $\langle \tau_{PL} \rangle$ value at the center was 5.5 ± 0.5 ns for Meso-TiO$_2$, and this value decreased to 3.4 ± 0.5 and 3.2 ± 0.6 ns for Au/Meso-TiO$_2$ and Pt/Meso-TiO$_2$, respectively. The observed shortening of emission lifetimes was also confirmed at the edge of Au/Meso-TiO$_2$ and Pt/Meso-TiO$_2$ (Supplementary Figure S7). The PL lifetime of Au/Meso-TiO$_2$ and Pt/Meso-TiO$_2$ remarkably reduced compared to bare Meso-TiO$_2$ because of the quenching of the PL by metal nanoparticles.

On the basis of the above data, we can make a simple calculation about electron diffusion coefficient (D_e) of metal/Meso-TiO$_2$. The Au/Meso-TiO$_2$ was chosen as a prototypical sample because most of the Au nanoparticles were loaded on the lateral surfaces of Meso-TiO$_2$. When TiO$_2$ is illuminated with UV light, e^-–h^+ pairs are generated. The electron (hole) trapping is very fast (femtoseconds to picoseconds) in regular TiO$_2$ and the trapped e^- and h^+ undergo a charge recombination process.[10−12,58,59] Since the e^- presumably migrates via trapping and detrapping processes in Meso-TiO$_2$ before recombination, the PL lifetime is inhomogeneous and widely distributed from tens of picoseconds to microseconds, or even up to milliseconds (ps to ms). In the case of Au/Meso-TiO$_2$, most of the photogenerated e^- were trapped by Au nanoparticles at the edge of Meso-TiO$_2$, thereby resulting in the observed PL quenching. The average rate constant for PL quenching by Au nanoparticles ($\langle k_q \rangle$) was calculated to be 1.3 × 10^8 s^{-1} by the equation[60] $\langle k_q \rangle = \langle \tau_{PL}(Au/Meso-TiO_2) \rangle^{-1} - \langle \tau_{PL}(Meso-TiO_2) \rangle^{-1}$. Since the electron migration from TiO$_2$ to the deposited metal should complete within a few picoseconds,[61,62] the observed PL quenching dynamics are likely related to the interparticle charge transfer processes. In terms of a simple two-dimensional random walk model, D_e can be estimated using $D_e = L_e^2/4\tau_e$, where L_e is the electron diffusion length and τ_e is the electron lifetime.[63] L_e is
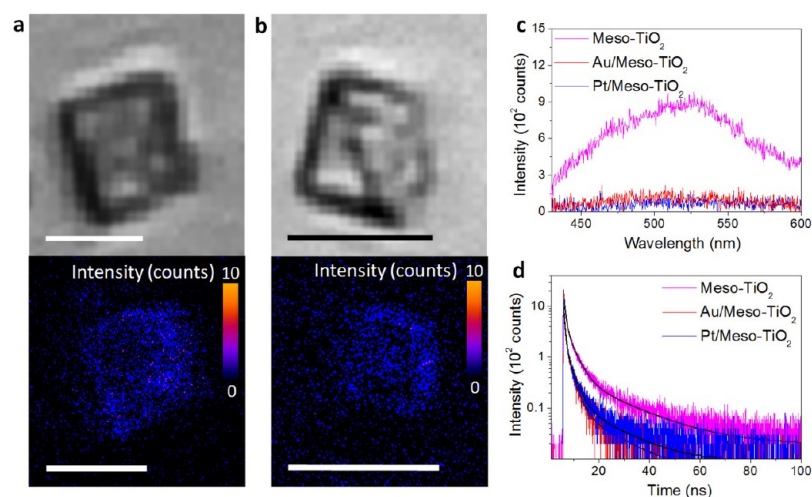
Figure 4. Optical transmission (upper side) and emission (under side) images of (a) 0.04 wt % Au/Meso-TiO$_2$ and (b) 1.0 wt % Pt/Meso-TiO$_2$ immobilized on a quartz glass (excitation wavelength, 380 nm; scale bars, 5 μm). (c) Emission spectra and (d) emission decay profiles observed at the center position on Meso-TiO$_2$, 0.04 wt % Au/Meso-TiO$_2$, and 1.0 wt % Pt/Meso-TiO$_2$.
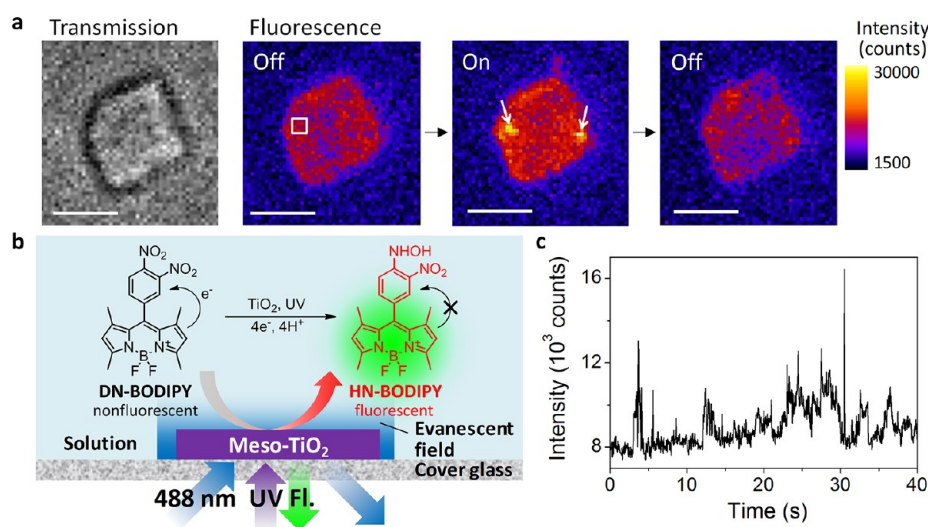

Figure 5. (a) Optical transmission of a 0.04 wt % Au/Meso-TiO$_2$ particle immobilized on a cover glass and fluorescence images of the same particle in Ar-saturated DN-BODIPY solution (0.5 mM in methanol) under 488 nm laser (I_{488} = 0.1 kW cm^{-2}) and UV irradiation (I_{UV} = 30 mW cm^{-2}). The fluorescence images display a series of successive images exhibiting on and off events (acquisition time, 50 ms). The arrows point out the location of fluorescence bursts. (b) Single-molecule fluorescence observation by TIRF microscopy and photocatalytic generation of fluorescent HN-BODIPY from nonfluorescent DN-BODIPY. (c) A typical profile of fluorescence intensity obtained from the white box marked in the fluorescence image (panel a). The scale bars are 2 μm.

considered to represent the effective detection length under the limit of optical diffraction (~300 nm), and τ_e is the reciprocal of the $\langle k_q \rangle$ value (7.7 ns). From these values, D_e was calculated to be 0.03 cm^2 s^{-1}. This value is more than 2 orders of magnitude higher than that reported for anatase TiO$_2$ nanocrystalline films (~10^{-4} cm^2 s^{-1})[64] and is even close to that for electrons *inside* anatase nanoparticles (~10^{-2} cm^2 s^{-1})[65] or anatase single crystal (~10^{-1} cm^2 s^{-1}).[66]

With the aim to demonstrate the interfacial electron transfer (ET) process on the surface of Meso-TiO$_2$, we performed single-molecule photocatalytic reduction of a probe molecule (3,4-dinitrophenyl-BODIPY, DN-BODIPY) over individual Meso-TiO$_2$ crystals by means of total internal reflection fluorescence (TIRF) microscopy (Figure 5b). This fluorogenic reaction is based on the ET-involved reduction of the dinitrophenyl group of DN-BODIPY.[67] Prior to reduction, the two nitro (NO$_2$) groups of the probe molecule significantly

decreased the lowest unoccupied molecular orbital (LUMO) energy level of the benzene moiety introduced at the meso position of the BODIPY core, thereby completely quenching the BODIPY fluorescence by an intramolecular ET from the excited fluorophore to the dinitrobenzene moiety. One of the NO$_2$ groups is reduced to a hydroxylamino (NHOH) moiety via multiple proton-coupled ET processes. The increased electron density is neutralized by the remaining NO$_2$ group, thereby suppressing the intramolecular ET process. Therefore, nonfluorescent DN-BODIPY ($\Phi_{fl} \approx 10^{-4}$ in methanol) can be reduced to form a highly fluorescent product (4-hydroxyamino-3-nitrophenyl-BODIPY, HN-BODIPY, Φ_{fl} = 0.50 in methanol) upon accepting electrons, and this reaction allows us to study the interfacial ET reaction on individual crystals via fluorescence detection of HN-BODIPY at the single-molecule level.[48,68]
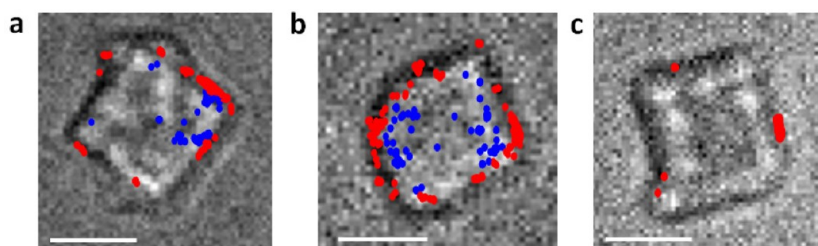
Figure 6. Transmission images of (a) Meso-TiO$_2$; (b) 0.04 wt % Au/Meso-TiO$_2$; and (c) 1.0 wt % Pt/Meso-TiO$_2$ immobilized on a cover glass in Ar-saturated methanol solution containing DN-BODIPY (0.5 μM) under both 488 nm laser and UV irradiation. The blue and red dots indicate the location of fluorescence bursts on the basal and lateral surfaces of the crystal, observed during 15 s of irradiation. The scale bars are 2 μm.

The photocatalytic activity of Meso-TiO$_2$ materials was first evaluated by using ensemble-averaged spectroscopy. We selected three photocatalysts, that is, Meso-TiO$_2$, 0.04 wt % Au/Meso-TiO$_2$, and 1.0 wt % Pt/Meso-TiO$_2$. When TiO$_2$ dispersions containing DN-BODIPY (15 μM, in Ar-saturated methanol) were exposed to 365 nm UV light, a new fluorescence peak appeared at ca. 510 nm, and the intensity of this peak remarkably increased with the irradiation time (Supplementary Figure S8). Note that this increase was negligible when no photocatalyst (control experiment) was present in the solution. Because the photogenerated h$^+$ in TiO$_2$ are efficiently scavenged by methanol, the photogenerated e$^-$ are primarily responsible for the reduction of DN-BODIPY to the fluorescent product HN-BODIPY; 0.04 wt % Au/Meso-TiO$_2$ exhibited the highest activity among the three samples under study. The reduction of DN-BODIPY over metal-nanoparticle-loaded Meso-TiO$_2$ preferentially takes place on the surface of metal nanoparticles versus bare TiO$_2$ surface as a result of the interfacial ET processes from TiO$_2$ to metals occurring on the surface.[68] According to the Langmuir–Hinshelwood model, the global reaction rate (i.e., the number of product molecules per unit of time) depends on the total number of adsorption sites (n_s) and the surface coverage (ϕ). As listed in Table 1, Au and Pt nanoparticles showed a comparable size, while the number of Pt nanoparticles was 8 times greater than that of Au. The lower observed reactivity of 1.0 wt % Pt/Meso-TiO$_2$ seems to be very rare given the higher metal loading of this sample. Wunder et al. recently showed that the adsorption equilibrium constant (K_{ad}) of 4-nitrophenol on the surface of Pt nanoparticles (2300 M^{-1}) is lower as compared to Au nanoparticles (5500 M^{-1}).[69] This implies that the adsorption energy of the nitro group, (a potential binding functionality[70]) on the Pt surface is lower than on Au. Although the direct comparison of K_{ad} for DN-BODIPY between Au and Pt nanoparticles is difficult as a result of the limited number of the product molecules detected in our experiments, it can be speculated that DN-BODIPY molecules have a similar or lower affinity to Pt nanoparticles on Meso-TiO$_2$ as compared to Au nanoparticles. In addition, photogenerated e$^-$ has priority to reduce hydrogen ions on the surface of Pt nanoparticles to generate hydrogen, thereby inhibiting formation of the fluorescent products.[50,71−73]

Figure 5a shows a typical TIRF image captured for a 0.04 wt % Au/Meso-TiO$_2$ crystal in Ar-saturated methanol containing DN-BODIPY under both a 488 nm laser and UV irradiation light. A number of fluorescence bursts with signals above the background level were observed during photoirradiation (Figure 5c and Supplementary Movie S1), and their locations were determined by using centroid analysis (see the dots in the optical transmission image of Figure 6). Control experiments confirmed that the simultaneous presence of the photocatalyst, DN-BODIPY, and the UV excitation light is essential to the generation of fluorescence bursts. During the course of single-molecule experiments, we noticed that some product molecules diffused inside the Meso-TiO$_2$ structure, which was not evident according to the bulk measurements (Supplementary Figure S9). This behavior was not observed for micrometer-sized TiO$_2$ single crystals,[48] thereby suggesting that this molecular diffusion is produced by the porous structures of Meso-TiO$_2$. A similar translation-diffusion behavior of single dye molecules was previously reported for porous TiO$_2$ nanotubes[74] and mesoporous silica.[75] With the aim to identify the location of the reaction sites, we only marked the fluorescence spots at which each fluorescent molecule first appeared. As shown in Figure 6a, most of the fluorescence spots were found to be located near the edge of Meso-TiO$_2$. This finding is qualitatively consistent with the observation that metal nanoparticles were preferentially photodeposited at the edge of Meso-TiO$_2$. The average reaction rates were estimated to be 5.6 and 11 molecules μm^{-2} s^{-1} for Meso-TiO$_2$, 2.3 and 19 molecules μm^{-2} s^{-1} for Au/Meso-TiO$_2$, and 0.5 and 1.6 molecules μm^{-2} s^{-1} for Pt/Meso-TiO$_2$ for the basal and lateral surfaces, respectively (Figure 6). Note that a similar tendency was observed for more than five individual crystals examined (Supplementary Figure S10 and Table S1). These results highlight a significant effect of the loading of noble metal nanoparticles, thereby opening the possibility to highly improve the photocatalytic activity of these materials. For instance, the average reaction rates decreased from 5.6 to 2.3 molecules μm^{-2} s^{-1} on the basal surfaces upon Au loading, whereas reaction rates increased from 11 to 19 molecules μm^{-2} s^{-1} on the lateral surfaces. These differences strongly support the herein proposed mechanism in which the photogenerated e$^-$ on the basal surfaces can rapidly migrate to the Au nanoparticles. As a special case, Pt/Meso-TiO$_2$ showed a relatively low activity toward the reduction of DN-BODIPY, which is highly consistent with the bulk experimental results (Supplementary Figure S8). However, reaction sites for reduction could still be preferentially distributed near the edge of Pt/Meso-TiO$_2$, thus inferring that most of the photogenerated e$^-$ in Pt/Meso-TiO$_2$ were transferred to the Pt nanoparticles.

We further examined the photocatalytic aqueous-phase oxidation of 4-chlorophenol (4-CP) and rhodamine B (RhB) as probe reactions to evaluate the photocatalytic activity of Meso-TiO$_2$, 0.04 wt % Au/Meso-TiO$_2$, and 1.0 wt % Pt/Meso-TiO$_2$ (Figure 7). No degradation was observed even after 4 h under dark or no photocatalyst conditions. However, no degradation of 4-CP was observed for Meso-TiO$_2$ and Au/Meso-TiO$_2$ after visible light irradiation (λ_{ex} > 430 nm; 140
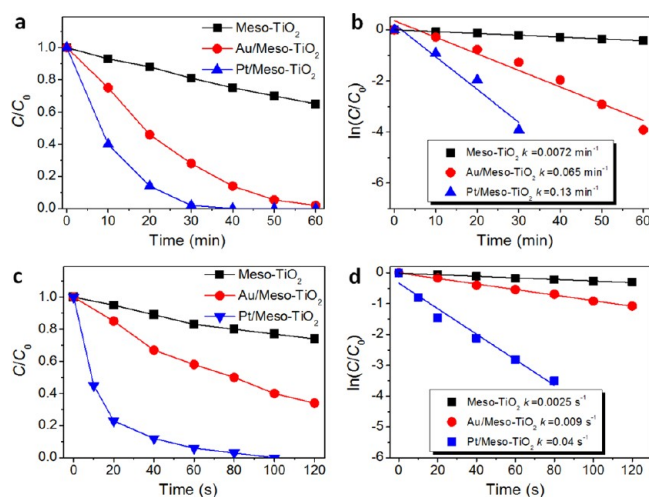
Figure 7. Liquid-phase photocatalytic degradation of (a) 4-CP and (c) RhB, and kinetic linear fitting curves of (b) 4-CP and (d) RhB over Meso-TiO$_2$, 0.04 wt % Au/Meso-TiO$_2$, and 1.0 wt % Pt/Meso-TiO$_2$ photocatalysts under UV light irradiation.
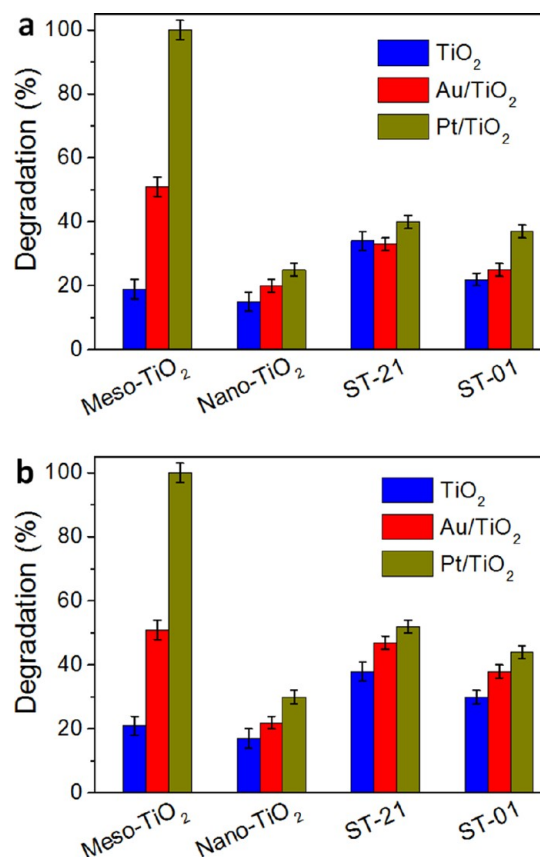

Figure 8. (a) Liquid-phase photocatalytic degradation and (b) total organic carbon (TOC) analyses of 4-CP oxidation on different photocatalysts (TiO$_2$, 0.04 wt % Au/TiO$_2$, and 1.0 wt % Pt/TiO$_2$) under UV light irradiation.

mW cm^{-1}) for 4 h; this result might exclude the involvement of electron or energy transfer from the excited Au nanoparticles to TiO$_2$. The conversion in the 4-CP oxidation reaction increased from 19% (Meso-TiO$_2$) to 72% (Au/Meso-TiO$_2$) and 100% (Pt/Meso-TiO$_2$) after 30 min of UV irradiation (Figure 7a), while, in the RhB oxidation reaction, the conversion enhanced from 23% to 60% and 100% after only 100 s of UV irradiation (Figure 7c). On the basis of a previous study,[76] the degradation of organics can be described by a pseudofirst-order reaction expression with a simplified Langmuir–Hinshelwood model when the adsorption equilibrium concentration of organics, C_0, is very low: $\ln(C_0/C_t) = kt$, where C_t is the concentration of organics at time t, and k is the apparent first-order rate constant. k for photodegradation of 4-CP was calculated to be 0.13 and 0.065 min^{-1} for Pt/Meso-TiO$_2$ and Au/Meso-TiO$_2$, respectively, which are much higher than that of Meso-TiO$_2$ (0.0072 min^{-1}, Figure 7b). Enhancements of about 9 and 18 times in k were observed after loading Au and Pt on Meso-TiO$_2$, respectively. Photodegradation of RhB showed similar results, with 3.6- and 16-fold increases in k, respectively (Figure 7d). This tremendous improvement in organics decomposition observed for Au/Meso-TiO$_2$ and Pt/Meso-TiO$_2$ unambiguously suggest that the efficient interfacial ET processes in the composites significantly improve their photocatalytic activity. Furthermore, the 1.0 wt % Pt/Meso-TiO$_2$ sample was used repetitively more than 8 times without significant deactivation, thereby indicating strong durability characteristics (Supplementary Figure S11).

We compared the activities of several Au/TiO$_2$ and Pt/TiO$_2$ samples with different loading amounts under the same conditions. With the aim to facilitate the comparison, the reference crystal phase of TiO$_2$ photocatalysts was anatase, including Nano-TiO$_2$[37] and commercial TiO$_2$ (ST-21, ST-01) samples. Meso-TiO$_2$-based Au/TiO$_2$ and Pt/TiO$_2$ composites showed the highest activity enhancements in both 4-CP and RhB oxidation (Figure 8a and Supplementary Figure S12). With the aim to evaluate the mineralization, we also analyzed the organics degradation by total organic carbon (TOC) measurements, and similar tendencies were found (Figure 8b). We believe that the main reason for this superior improvement of the Meso-TiO$_2$ photoactivity lies in its particular structure.

More specifically, the noble metal nanoparticles on Meso-TiO$_2$ can efficiently collect the photogenerated e$^-$ through the conductive network in the superstructure of TiO$_2$ nanocrystals, thereby leading to increased charge separation efficiency and the corresponding inhibition of e$^-$ and h$^+$ charge recombination processes.

Finally, we compared the loading amounts of different Au/TiO$_2$ and Pt/TiO$_2$ samples required to reach the same degree of photocatalytic activity (Supplementary Figures S13 and S14). Table 1 lists the loading amounts of noble metals required to reach 50% of photocatalytic degradation of 4-CP under the same experimental conditions. It should be noted that the optimum loading amounts of metals on Meso-TiO$_2$ were about 10 times lower than those of other TiO$_2$ samples. ST-01, however, was an exception because it has a very small particle size. The particle sizes of TiO$_2$, Au, and Pt were determined by TEM and used to calculate the number of Au (N_{Au}) or Pt (N_{Pt}) nanoparticles per TiO$_2$ nanoparticle (Supplementary Figure S15 and Table 1). N_{Au} and N_{Pt} of the Meso-TiO$_2$-based composites were 0.01 and 0.08, respectively, which were much lower than those of other composites except in the case of ST-01. These results indicate that the superstructure of TiO$_2$ allows remarkable reduction in noble metal loading while preserving a high photocatalytic activity. This is very important for practical use of TiO$_2$ photocatalysts because of the high price of noble metals.

CONCLUSIONS

In summary, we studied the PL and photocatalytic properties of Meso-TiO$_2$ loaded with noble metal nanoparticles. The electron transport distance on the superstructure of TiO$_2$ was found in the micrometer distance. Furthermore, the calculation of D_e on Meso-TiO$_2$ was higher than that reported for anatase TiO$_2$ nanocrystalline films, thus emphasizing the importance of the ordered alignment in TiO$_2$ nanocrystals. The single-particle, single-molecule experiments clearly revealed that the photogenerated e$^-$ are preferentially trapped at the edge of Meso-TiO$_2$, where {101} facets are predominantly exposed. This anisotropic electron flow in the superstructure significantly retarded the charge recombination with h$^+$, thereby resulting in an enhanced (up to 10 times) photocatalytic oxidation activity. Moreover, Meso-TiO$_2$ samples required much lower loadings of noble metals to reach the same photocatalytic activity than standard TiO$_2$ samples. This is highly beneficial to design and fabricate novel photoactive materials for practical applications such as photocatalysis, photoelectrochemical water splitting, or dye-sensitized solar cells (DSSCs). We believe that our methodology and approach can be applied to other semiconductor superstructures and their composites.

EXPERIMENTAL METHODS

Preparation of Au or Pt nanoparticle-Loaded TiO$_2$. Meso-TiO$_2$ and Nano-TiO$_2$ (annealed under oxygen atmosphere at 500 °C) were synthesized according to literature procedures.[37,77] X-ray photoelectron spectroscopy (XPS) spectra confirmed that the impurities (such as N or F) on the TiO$_2$ surface are almost entirely removed after annealing.[37] Commercial ST-21 and ST-01 (Ishihara Sangyo) were used as received. In a typical synthesis, 0.25 g TiO$_2$, 225 mL of Milli-Q ultrapure water (Millipore), 25 mL methanol, and a certain amount of HAuCl$_4$ or H$_2$PtCl$_6$ (Aldrich) were mixed forming a homogeneous suspension. The solutions were then exposed to UV light from a mercury light source (Asahi Spectra, REX-120) for 30 min at room temperature. Finally, the solutions were centrifuged at 10 000 rpm (Hitachi, himac CF16RX) to separate the solid products. The products were subsequently calcined in air (20 °C min^{-1}) at 500 °C (Au/TiO$_2$) or 300 °C (Pt/TiO$_2$) for 30 min. The amounts of loaded metals were determined by inductively coupled plasma (ICP) emission spectroscopy (Shimadzu, ICPS-8100).

Instruments. The samples were characterized using X-ray diffraction (XRD, Rigaku Rint-2500, CuKα source), SEM (JEOL JSM-6330FT), and TEM (JEOL JEM 3000F, operated at 300 kV). The steady-state UV−visible absorption and diffuse reflectance spectra were measured by UV−visible/near-infrared spectrophotometers (Shimadzu, UV-3100, and Jasco, V-570, respectively) at room temperature. The steady-state fluorescence spectra were measured using a HORIBA FluoroMax-4 fluorescence spectrophotometer.

Single-Particle PL Measurements with Time-Resolved Confocal Mcroscopy. The quartz cover glasses were purchased from DAICO MFG CO., Ltd. (Japan) and cleaned by sonication in a 20% detergent solution (As One, Cleanace) for 6 h, followed by repeated washings with warm flowing water for 30 min. Finally, the cover glasses were washed again with Milli-Q ultrapure water (Millipore). Well-dispersed aqueous suspensions of TiO$_2$ were subsequently spin-coated on the cleaned cover glasses. The cover glasses were annealed at 100 °C for 1 h to immobilize the particles on the glass surface.

Single-particle PL images and lifetimes were recorded using an objective-scanning confocal microscope system (PicoQuant, MicroTime 200) coupled with an Olympus IX71 inverted fluorescence microscope.[48] The samples were excited through an oil objective (Olympus, UPLSAPO 100XO; 1.40 NA, 100×) with a circular-polarized 380 nm pulsed laser (Spectra-Physics, MAI TAI HTS-W provided with an automated frequency doubler, Inspire Blue FAST-W; 0.8 MHz repetition rate, 10 μW excitation power) controlled by a PDL-800B driver (Pico-Quant). An instrument response function (IRF) of ∼100 ps was obtained by measuring the scattered laser light in order to analyze the temporal profile. The emission was collected with the same objective and detected by a single photon avalanche photodiode (Micro Photon Devices, PDM 50CT) through a dichroic beam splitter (Chroma, z405/488rpc), a long-pass filter (Chroma, HQ510LP), and a 50 μm pinhole for spatial filtering to reject out-of-focus signals. The data collected using the PicoHarp 300 TCSPC module (PicoQuant) were stored in the time-tagged time-resolved mode (TTTR), recording every detected photon with its individual timing, which were used for the single-molecule analysis. For the spectroscopy, only the emission that passed through a slit entered the imaging spectrograph (ActonResearch, SP-2356) that was equipped with an electron-multiplying charge-coupled device (EMCCD) camera (Princeton Instruments, ProEM). The spectra were typically integrated for 30 s. The spectrum detected by the EMCCD camera was stored and analyzed by using a personal computer. All the experimental data were obtained at room temperature.

Single-Molecule Fluorescence Measurements with Wide-Field Microscopy. The sample preparation and detailed experimental and analytical procedures were described elsewhere.[48] The experimental setup included an Olympus IX81 inverted fluorescence microscope; 488 nm CW laser (OZ Optics; 0.1 kWcm^{-2} at the glass surface) and 365 nm LED (Opto-Line; 30 mW cm^{-2} at the glass surface) sources were used to excite the dyes and TiO$_2$, respectively. The transmission and emission images were recorded on an EMCCD camera (Roper Scientific, Evolve 512) at a frame rate of 20 frames s^{-1} using MetaMorph (Molecular Devices). All experimental data were obtained at room temperature. With the aim to determine the locations of the reactive site distributed on the surface, the precise positions of the fluorescent spots were analyzed for each image using the ImageJ software (http://rsb.info.nih.gov/ij/) with an octane plugin.[78]

Photocatalytic Activity Tests. For typical photocatalytic runs, 2 mL of a TiO$_2$ dispersion (0.5 g/L) containing an aqueous solution (4-CP, 1.0 × 10^{-4} M; RhB, 1.0 × 10^{-5} M) was sonicated for 20 min and then transferred into a quartz cuvette. The photocatalytic reaction was initiated upon irradiation with a mercury light source (Asahi Spectra, REX-120) through a filter (centered at 365 nm) at room temperature. The intensity of the UV light was measured to be about 140 mW cm^{-2}. The reaction time was 30 min for 4-CP and 100 s for RhB. After stopping the UV illumination, the sample was centrifuged at 10 000 rpm (Hitachi, himac CF16RX) to separate the solid particles. The concentration of unreacted molecules, from which the degradation yield was calculated, was analyzed by a UV spectrophotometer (Shimadzu, UV-3100) at their characteristic wavelength. The mineralization of 4-CP was followed by monitoring the total

organic carbon (TOC) with a TOC analyzer (Shimadzu, TOC-VCSH).

■ AUTHOR INFORMATION

Corresponding Author

*E-mail: tachi45@sanken.osaka-u.ac.jp (T.T.); majima@sanken.osaka-u.ac.jp (T.M.).

Notes

The authors declare no competing financial interest.

■ REFERENCES

(1) Costi, R.; Saunders, A. E.; Banin, U. *Angew. Chem., Int. Ed.* **2010**, *49*, 4878−4897.

(2) Kamat, P. V. *J. Phys. Chem. C* **2007**, *111*, 2834−2860.

(3) Redl, F. X.; Cho, K. S.; Murray, C. B.; O'Brien, S. *Nature* **2003**, *423*, 968−971.

(4) Lee, J.; Govorov, A. O.; Dulka, J.; Kotov, N. A. *Nano Lett.* **2004**, *4*, 2323−2330.

(5) Tada, H.; Mitsui, T.; Kiyonaga, T.; Akita, T.; Tanaka, K. *Nat. Mater.* **2006**, *5*, 782−786.

(6) Murdoch, M.; Waterhouse, G. I. N.; Nadeem, M. A.; Metson, J. B.; Keane, M. A.; Howe, R. F.; Llorca, J.; Idriss, H. *Nat. Chem.* **2011**, *3*, 489−492.

(7) Gong, X. Q.; Selloni, A.; Dulub, O.; Jacobson, P.; Diebold, U. *J. Am. Chem. Soc.* **2008**, *130*, 370−381.

(8) Fujishima, A.; Rao, T. N.; Tryk, D. A. *J. Photochem. Photobiol., C* **2000**, *1*, 1−21.

(9) Chen, X.; Mao, S. S. *Chem. Rev.* **2007**, *107*, 2891−2959.

(10) Rothenberger, G.; Moser, J.; Grätzel, M.; Serpone, N.; Sharma, D. K. *J. Am. Chem. Soc.* **1985**, *107*, 8054−8059.

(11) Tamaki, Y.; Hara, K.; Katoh, R.; Tachiya, M.; Furube, A. *J. Phys. Chem. C* **2009**, *113*, 11741−11746.

(12) Tachikawa, T.; Fujitsuka, M.; Majima, T. *J. Phys. Chem. C* **2007**, *111*, 5259−5275.

(13) Zhang, Z. B.; Wang, C. C.; Zakaria, R.; Ying, J. Y. *J. Phys. Chem. B* **1998**, *102*, 10871−10878.

(14) Wu, N. Q.; Wang, J.; Tafen, D.; Wang, H.; Zheng, J. G.; Lewis, J. P.; Liu, X. G.; Leonard, S. S.; Manivannan, A. *J. Am. Chem. Soc.* **2010**, *132*, 6679−6685.

(15) Yang, D. J.; Liu, H. W.; Zheng, Z. F.; Yuan, Y.; Zhao, J. C.; Waclawik, E. R.; Ke, X. B.; Zhu, H. Y. *J. Am. Chem. Soc.* **2009**, *131*, 17885−17893.

(16) Teoh, W. Y.; Scott, J. A.; Amal, R. *J. Phys. Chem. Lett.* **2012**, *3*, 629−639.

(17) Sun, B.; Vorontsov, A. V.; Smirniotis, P. G. *Langmuir* **2003**, *19*, 3151−3156.

(18) Subramanian, V.; Wolf, E. E.; Kamat, P. V. *J. Am. Chem. Soc.* **2004**, *126*, 4943−4950.

(19) Tada, H.; Soejima, T.; Ito, S.; Kobayashi, H. *J. Am. Chem. Soc.* **2004**, *126*, 15952−15953.

(20) Li, H. X.; Bian, Z. F.; Zhu, J.; Huo, Y. N.; Li, H.; Lu, Y. F. *J. Am. Chem. Soc.* **2007**, *129*, 4538−4539.

(21) Jakob, M.; Levanon, H.; Kamat, P. V. *Nano Lett.* **2003**, *3*, 353−358.

(22) Cushing, S. K.; Li, J.; Meng, F.; Senty, T. R.; Suri, S.; Zhi, M.; Li, M.; Bristow, A. D.; Wu, N. *J. Am. Chem. Soc.* **2012**, *134*, 15033−15041.

(23) Atwater, H. A.; Polman, A. *Nat. Mater.* **2010**, *9*, 205−213.

(24) Christopher, P.; Ingram, D. B.; Linic, S. *J. Phys. Chem. C* **2010**, *114*, 9173−9177.

(25) Hu, C.; Peng, T.; Hu, X.; Nie, Y.; Zhou, X.; Qu, J.; He, H. *J. Am. Chem. Soc.* **2010**, *132*, 857−862.

(26) Ingram, D. B.; Linic, S. *J. Am. Chem. Soc.* **2011**, *133*, 5202−5205.

(27) Kowalska, E.; Mahaney, O. O. P.; Abe, R.; Ohtani, B. *Phys. Chem. Chem. Phys.* **2010**, *12*, 2344−2355.

(28) Tian, Y.; Tatsuma, T. *Chem. Commun.* **2004**, 1810−1811.

(29) Kong, M.; Li, Y. Z.; Chen, X.; Tian, T. T.; Fang, P. F.; Zheng, F.; Zhao, X. J. *J. Am. Chem. Soc.* **2011**, *133*, 16414−16417.

(30) Lakshminarasimhan, N.; Bae, E.; Choi, W. *J. Phys. Chem. C* **2007**, *111*, 15244−15250.

(31) Lakshminarasimhan, N.; Kim, W.; Choi, W. *J. Phys. Chem. C* **2008**, *112*, 20451−20457.

(32) Choi, S. K.; Kim, S.; Lim, S. K.; Park, H. *J. Phys. Chem. C* **2010**, *114*, 16475−16480.

(33) Ismail, A. A.; Bahnemann, D. W. *J. Phys. Chem. C* **2011**, *115*, 5784−5791.

(34) Tirosh, S.; Dittrich, T.; Ofir, A.; Grinis, L.; Zaban, A. *J. Phys. Chem. B* **2006**, *110*, 16165−16168.

(35) Gonzalez-Vazquez, J. P.; Morales-Florez, V.; Anta, J. A. *J. Phys. Chem. Lett.* **2012**, *3*, 386−393.

(36) Zhou, L.; Smyth-Boyle, D.; O'Brien, P. *J. Am. Chem. Soc.* **2008**, *130*, 1309−1320.

(37) Bian, Z.; Tachikawa, T.; Majima, T. *J. Phys. Chem. Lett.* **2012**, *3*, 1422−1427.

(38) Penn, R. L.; Banfield, J. F. *Geochim. Cosmochim. Acta* **1999**, *63*, 1549−1557.

(39) Buonsanti, R.; Carlino, E.; Giannini, C.; Altamura, D.; De Marco, L.; Giannuzzi, R.; Manca, M.; Gigli, G.; Cozzoli, P. D. *J. Am. Chem. Soc.* **2011**, *133*, 19216−19239.

(40) Etgar, L.; Moehl, T.; Gabriel, S.; Hickey, S. G.; Eychmuller, A.; Gratzel, M. *ACS Nano* **2012**, *6*, 3092−3099.

(41) Mics, Z.; Nemec, H.; Rychetsky, I.; Kuzel, P.; Formanek, P.; Maly, P.; Nemec, P. *Phys. Rev. B: Condens. Matter Mater. Phys.* **2011**, *83*, 155326/1−155326/6.

(42) Nemec, H.; Rochford, J.; Taratula, O.; Galoppini, E.; Kuzel, P.; Polivka, T.; Yartsev, A.; Sundstrom, V. *Phys. Rev. Lett.* **2010**, *104*, 197401/1−197401/4.

(43) Tachikawa, T.; Majima, T. *Chem. Soc. Rev.* **2010**, *39*, 4802−4819.

(44) De Cremer, G.; Sels, B. F.; De Vos, D. E.; Hofkens, J.; Roeffaers, M. B. J. *Chem. Soc. Rev.* **2010**, *39*, 4703−4717.

(45) Chen, P.; Zhou, X.; Shen, H.; Andoy, N. M.; Choudhary, E.; Han, K.-S.; Liu, G.; Meng, W. *Chem. Soc. Rev.* **2010**, *39*, 4560−4570.

(46) Ohno, T.; Sarukawa, K.; Matsumura, M. *New J. Chem.* **2002**, *26*, 1167−1170.

(47) Murakami, N.; Kurihara, Y.; Tsubota, T.; Ohno, T. *J. Phys. Chem. C* **2009**, *113*, 3062−3069.

(48) Tachikawa, T.; Yamashita, S.; Majima, T. *J. Am. Chem. Soc.* **2011**, *133*, 7197−7204.

(49) D'Arienzo, M.; Carbajo, J.; Bahamonde, A.; Crippa, M.; Polizzi, S.; Scotti, R.; Wahba, L.; Morazzoni, F. *J. Am. Chem. Soc.* **2011**, *133*, 17652−17661.

(50) Wood, A.; Giersig, M.; Mulvaney, P. *J. Phys. Chem. B* **2001**, *105*, 8810−8815.

(51) Bian, Z. F.; Zhu, J.; Cao, F. L.; Lu, Y. F.; Li, H. X. *Chem. Commun.* **2009**, 3789−3791.

(52) Jeon, K.-S.; Oh, S.-D.; Suh, Y. D.; Yoshikawa, H.; Masuhara, H.; Yoon, M. *Phys. Chem. Chem. Phys.* **2009**, *11*, 534−542.

(53) Tachikawa, T.; Ishigaki, T.; Li, J.-G.; Fujitsuka, M.; Majima, T. *Angew. Chem., Int. Ed.* **2008**, *47*, 5348−5352.

(54) Tachikawa, T.; Majima, T. *J. Am. Chem. Soc.* **2009**, *131*, 8485−8495.

(55) Knorr, F. J.; Zhang, D.; McHale, J. L. *Langmuir* **2007**, *23*, 8686−8690.

(56) Beveratos, A.; Brouri, R.; Gacoin, T.; Poizat, J.-P.; Grangier, P. *Phys. Rev. A: At., Mol., Opt. Phys.* **2001**, *64*, 061802/1−061802/4.

(57) Kiyonaga, T.; Fujii, M.; Akita, T.; Kobayashi, H.; Tada, H. *Phys. Chem. Chem. Phys.* **2008**, *10*, 6553−6561.

(58) Bahnemann, D. W.; Hilgendorff, M.; Memming, R. *J. Phys. Chem. B* **1997**, *101*, 4265−4275.

(59) Furube, A.; Asahi, T.; Masuhara, H.; Yamashita, H.; Anpo, M. *J. Phys. Chem. B* **1999**, *103*, 3120−3127.

(60) Robel, I.; Kuno, M.; Kamat, P. V. *J. Am. Chem. Soc.* **2007**, *129*, 4136−4137.

(61) Furube, A.; Asahi, T.; Masuhara, H.; Yamashita, H.; Anpo, M. *Chem. Phys. Lett.* **2001**, *336*, 424−430.

(62) Iwata, K.; Takaya, T.; Hamaguchi, H.; Yamakata, A.; Ishibashi, T.; Onishi, H.; Kuroda, H. *J. Phys. Chem. B* **2004**, *108*, 20233−20239.

(63) Frank, A. J.; Kopidakis, N.; van de Lagemaat, J. *Coord. Chem. Rev.* **2004**, *248*, 1165−1179.

(64) Nakade, S.; Saito, Y.; Kubo, W.; Kitamura, T.; Wada, Y.; Yanagida, S. *J. Phys. Chem. B* **2003**, *107*, 8607−8611.

(65) Enright, B.; Fitzmaurice, D. *J. Phys. Chem.* **1996**, *100*, 1027−1035.

(66) Kopidakis, N.; Benkstein, K. D.; van de Lagemaat, J.; Frank, A. J.; Yuan, Q.; Schiff, E. A. *Phys. Rev. B: Condens. Matter Mater. Phys.* **2006**, *73*, 045326.

(67) Tachikawa, T.; Wang, N.; Yamashita, S.; Cui, S.-C.; Majima, T. *Angew. Chem., Int. Ed.* **2010**, *49*, 8593−8597.

(68) Wang, N.; Tachikawa, T.; Majima, T. *Chem. Sci.* **2011**, *2*, 891−900.

(69) Wunder, S.; Polzer, F.; Lu, Y.; Mei, Y.; Ballauff, M. *J. Phys. Chem. C* **2010**, *114*, 8814−8820.

(70) Gao, P.; Weaver, M. J. *J. Phys. Chem.* **1985**, *89*, 5040−5046.

(71) Nosaka, Y.; Norimatsu, K.; Miyama, H. *Chem. Phys. Lett.* **1984**, *106*, 128−131.

(72) Bamwenda, G. R.; Tsubota, S.; Nakamura, T.; Haruta, M. *J. Photochem. Photobiol., A* **1995**, *89*, 177−189.

(73) Grimme, R. A.; Lubner, C. E.; Bryant, D. A.; Golbeck, J. H. *J. Am. Chem. Soc.* **2008**, *130*, 6308−6309.

(74) Naito, K.; Tachikawa, T.; Fujitsuka, M.; Majima, T. *J. Am. Chem. Soc.* **2009**, *131*, 934−936.

(75) Zürner, A.; Kirstein, J.; Döblinger, M.; Bräuchle, C.; Bein, T. *Nature* **2007**, *450*, 705−708.

(76) Al-Ekabi, H.; Serpone, N. *J. Phys. Chem.* **1988**, *92*, 5726−5731.

(77) Zhu, J.; Wang, S.; Bian, Z.; Xie, S.; Cai, C.; Wang, J.; Yang, H.; Li, H. *CrystEngComm* **2010**, *12*, 2219−2224.

(78) Niu, L.; Yu, J. *Biophys. J.* **2008**, *95*, 2009−2016.

25453

dx.doi.org/10.1021/jp309683f | *J. Phys. Chem. C* 2012, 116, 25444−25453